Chinese Chemical Letters 37 (2026) 112479

Contents lists available at ScienceDirect

Chinese Chemical Letters

journal homepage: www.elsevier.com/locate/cclet

Ni sites enhanced dual-Prussian blue analogs S-scheme photocatalyst for efficient CO_2 reduction

Enqi Zhang[a,1], Fanyu Kong[a,1], Lina Dai[a], Xianglan Dong[a], Hongquan Jiang[a,*], Yanduo Liu[a,*], Yang Qu[b,*]

[a] School of Chemistry and Chemical Engineering, Harbin Normal University, Harbin 150025, China
[b] Key Laboratory of Functional Inorganic Materials Chemistry (Ministry of Education), School of Chemistry and Materials Science, International Joint Research Center for Catalytic Technology, Heilongjiang University, Harbin 150080, China

ARTICLE INFO

Article history:
Received 29 August 2025
Revised 22 January 2026
Accepted 29 January 2026
Available online 29 January 2026

Keywords:
Zn-Co PBAs
Ni-Co PBAs
CO_2 reduction
S-scheme heterojunction

ABSTRACT

Photocatalytic CO_2 reduction is a cutting-edge technology with significant strategic importance for mitigating climate change and advancing energy transitions. In this study, we developed a high-performance photocatalyst by constructing a tightly interfaced S-scheme heterojunction from Prussian blue analogs (PBAs). Using $[Co^{2+}(CN)_6]^{4-}$ as the base, we selected two PBAs with high energy-level matching and connected them *via* M-NC-Co-CN-M bonds. Experimental results showed that the optimized Ni/Zn-Co PBAs S-scheme photocatalyst achieved a CO_2 conversion rate of ~38 μmol g^{-1} h^{-1} (94.13 % CO and 5.87 % CH_4). This design effectively improved the utilization efficiency of photogenerated charges and enhanced redox capabilities, while the Ni site further boosted CO_2 activation. This study not only offers new insights into designing efficient PBA-based photocatalysts but also demonstrates the promise of S-scheme mechanism in improving photocatalytic CO_2 reduction activity.

© 2026 Published by Elsevier B.V. on behalf of Chinese Chemical Society and Institute of Materia Medica, Chinese Academy of Medical Sciences.

Research into photocatalytic CO_2 reduction holds significant strategic importance for addressing global climate change, reshaping energy structures, and driving technological innovation [1,2]. As atmospheric CO_2 concentrations surpass 420 ppm, this technology mimics natural photosynthesis to efficiently convert CO_2 into valuable fuels (CO and CH_4). Beyond directly reducing greenhouse gas levels, it establishes a new paradigm for artificial carbon cycling. Studies suggest that converting just 10 % of global CO_2 emissions through photocatalysis could offset three months of human carbon emissions, making it a critical pathway toward achieving carbon neutrality [3,4]. Additionally, advancements in this field have spurred interdisciplinary research in materials science, catalytic chemistry, and energy science, providing theoretical foundations for designing efficient photocatalysts and optimizing reaction mechanisms [5,6]. By enabling carbon resource recycling and promoting low-carbon energy transitions, photocatalytic CO_2 reduction furnishes an encouraging solution for building a sustainable and carbon-neutral future.

To address the extremely short lifetime of photoexcited carriers in single semiconductor, a common strategy is to combine two schemes of photocatalysts. Experimental results have shown that this approach can enhance photocatalytic activity. While type-II and Z-scheme mechanisms have been submitted to explain the thorny issue, neither the thermodynamic energy loss nor the kinetic charge repulsion in these models adequately accounts for the observed enhancements [7,8]. To resolve these limitations, scientists introduced a novel concept: S-scheme heterojunction [9,10]. This concept provides a clear description of electron transfer from lower-energy states to higher-energy states. When a reductive photocatalyst with a higher Fermi level and bandgap structure is brought into contact with an oxidative photocatalyst, the photoexcited electrons in the conduction band (CB) of the oxidative phase are selectively injected into the valence band (VB) of the reductive partner, thereby suppressing bulk recombination, under the combined effects of this built-in electric field [11–13]. Meanwhile, the remaining photoexcited carriers are retained in the reductive partner CB and the oxidative phase VB. This S-scheme heterojunction achieves highly efficient charge separation and exhibits robust photoredox capabilities, thereby significantly enhancing photocatalytic performance.

Prussian blue analogs (PBAs) are stable coordination polymers that fall under the broader category of MOFs [14,15]. Their struc-

* Corresponding authors.
E-mail addresses: h.q.jiang1119@163.com (H. Jiang), liuyd0608@163.com (Y. Liu), quyang@hlju.edu.cn (Y. Qu).
[1] These authors contributed equally to this work.

https://doi.org/10.1016/j.cclet.2026.112479
1001-8417/© 2026 Published by Elsevier B.V. on behalf of Chinese Chemical Society and Institute of Materia Medica, Chinese Academy of Medical Sciences.

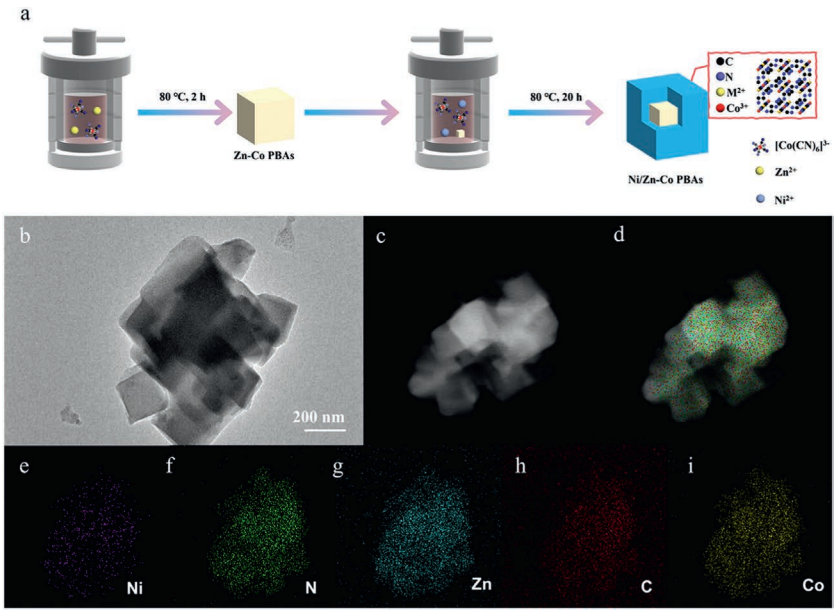


Fig. 1. (a) Synthetic pathway of the Ni/Zn dual-PBAs. (b-i) Transmission electron microscope (TEM) image and energy dispersive X-ray spectroscopy (EDX) mapping of Ni/Zn-Co PBAs.

tural tunability enhances carrier charge separation and transport rates, while their high porosity provides ample active sites and adsorption channels [16]. These advantages make PBAs superior to many MOFs (*e.g.*, ZIFs, UiO-66) in terms of light absorption range, charge transport rates, and CO_2 adsorption capacity. Compared with traditional photocatalysts, PBAs exhibit unique ligand field effects and diverse metal centers [17,18]. Due to these properties, PBAs have been widely applied in photocatalysis.

The bandgap structure of PBAs is closely related to their structure and electronic properties [19,20]. By modulating the electronic structure, the band positions and bandgap width of PBAs can be effectively tuned. For PBAs with the general formula $M_1[M_2(CN)_6]_x{\cdot}yH_2O$, regulating the M_1 site and its coordination environment is the most effective strategy for controlling their band structure [21,22]. Additionally, PBAs exhibit strong visible-light absorption, which is primarily influenced by the D-electron count of the metal centers, especially at the M_1 site [23]. So, when tuning the metal centers, both their redox capabilities and visible-light absorption range should be considered to identify PBAs with broad spectral responses, paving the way for the creation of exceptionally efficient photocatalytic systems.

Based on the above analysis, we used $[Co^{2+}(CN)_6]^{4-}$ as the foundation and selected various M_1 metal sites to screen the band structure of PBA-based photocatalysts. On this basis, we chose two PBAs with high energy-level matching and connected them *via* M-NC-Co-CN-M bonds. By modulating the interfacial electronic structure with these chemical bonds, we constructed a closely contacted PBAs-based S-scheme photocatalyst, enabling stepwise transfer of photogenerated charges between the two PBAs. Among them, the optimal Ni/Zn-Co PBAs S-scheme photocatalyst exhibited a CO_2 conversion performance of ~38 μmol g^{-1} h^{-1} (94.13 % CO and 5.87 % CH_4). This design effectively improved the utilization efficiency of photogenerated charges and enhanced redox capabilities, while the Ni site further boosted CO_2 activation. This work opens up an innovative avenue toward designing high-performance PBAs-based S-scheme system but also paves the way for sustainable carbon utilization technologies.

The synthesis process of the Ni/Zn-Co PBAs cubic S-scheme photocatalyst is shown in Fig. 1a. The Zn-Co PBAs cubic photocatalyst is prepared by controlling the pH value using a structure-directing agent. To obtain Zn-Co PBAs cubes with a regular structure and uniform size, sodium citrate is selected as the structure-directing agent. The charge diffusion distance between heterojunction interfaces typically ranges from a few nanometers to tens of nanometers, and the regulation of the interface structure determines the charge transfer capability and photocatalytic performance of the S-scheme heterostructure. To achieve a closely integrated interface for rapid and smooth spatial charge transfer, the Zn-Co PBAs cubic photocatalyst is used as the core, and an *in-situ* growth technique is employed to uniformly coat Ni-Co PBAs on the surface of Zn-Co PBAs cubic photocatalysts (Ni/Zn-Co PBAs) through a Ni-N-C-Co-C-N-Zn structure [19,21,23]. It is observed that the edge length of the Ni/Zn-Co PBAs cubic S-scheme photocatalyst increases from ~160 nm to ~200 nm (Fig. 1b and Fig. S1 in Supporting information). Additionally, Ni/Zn-Co PBAs cubic S-scheme photocatalyst was further determined by elemental distribution (Figs. 1c-i). It can be seen that Zn, the main element of the Zn-Co PBAs core, is concentrated in the central area of the composite sample. In contrast, the corresponding Ni element is sparsely distributed in the edge and peripheral positions. Furthermore, since both Zn-Co PBAs and Ni-Co PBAs belong to Co-based PBAs and share the same crystalline structure, their XRD characteristic peaks are identical (Fig. S2a in Supporting information). However, compared with Zn-Co PBAs, Ni-Co PBAs exhibits significant light absorption in the near-infrared region, resulting in visible light response in Ni/Zn-Co PBAs due to the Ni-Co PBAs coating, thereby extending the near-infrared light absorption capability of Zn-Co PBAs (Fig. S2b in Supporting information).

Orthogonal experiments, an efficient multi-factor experimental design method, allow for a comprehensive investigation of the effects of multiple factors and their interactions on experimental outcomes with minimal experimental runs through orthogonal arrays. Using orthogonal experiments, the most significant reaction conditions affecting the photocatalytic performance of 4Ni/Zn-Co PBAs were rapidly and systematically identified (Figs. 2a-c). Based on these optimized conditions, the CO_2 reduction performance of five Co-based PBAs monomers (Fig. S3a and Table S1 in Supporting information), Co-based PBAs composite photocatalysts conforming to the S-scheme mechanism (Fig. S3b and Table S2 in Supporting information), and xNi/Zn-Co PBAs composite photocatalysts

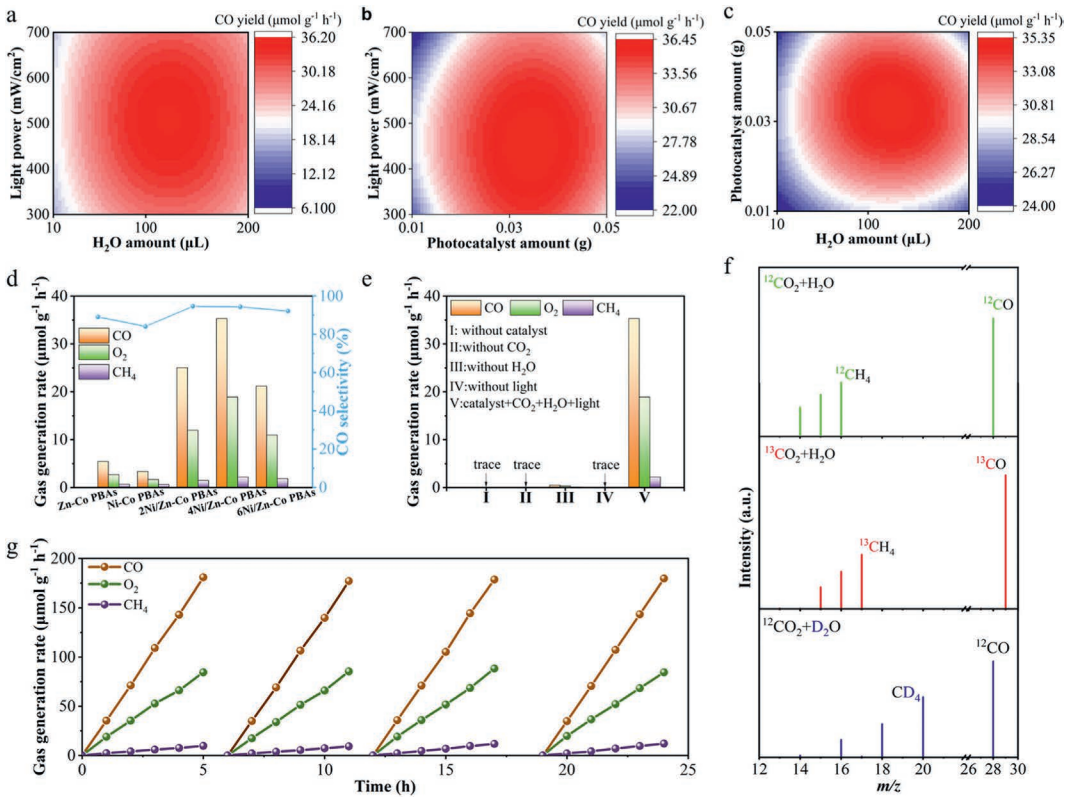


Fig. 2. (a-c) The effects of reaction conditions on the performance of 4Ni/Zn-Co PBAs. (d) The photocatalytic performance of various photocatalysts. (e) Comparative experiments, (f) isotopic data, and (g) stability tests over 4Ni/Zn-Co PBAs.

(Fig. 2d and Table S3 in Supporting information) was tested. The results showed that Co-based PBAs composite photocatalysts conforming with the S-scheme mechanism significantly improved CO_2 reduction performance. Among them, 4Ni/Zn-Co PBAs, based on the best-performing monomer Zn-Co PBAs, exhibited the highest CO generation rate, achieving a CO_2 conversion yield of ~38 μmol g^{-1} h^{-1} (94.13 % CO and 5.87 % CH_4). Compared with other systems near years, the Ni/Zn-Co PBAs cubic S-scheme photocatalyst demonstrated advantages in both selectivity and conversion rate (Table S4 in Supporting information). Notably, in all samples, the molar ratio of O_2 to carbon-containing products was nearly 1:2, indicating strict stoichiometric reactions during CO_2 conversion without accompanying side reactions.

To verify the roles of each component in the reaction system and the origin of the products, blank control experiments (Fig. 2e) and isotope labeling experiments (Fig. 2f) were conducted using 4Ni/Zn-Co PBAs as the target. The results showed that the effective conversion of CO_2 could not be achieved if any component, photocatalyst, H_2O, CO_2, or light source, was missing. Similarly, when substituting with $^{13}CO_2$ and D_2O, the corresponding products changed, confirming that the CO_2 conversion products were exclusively derived from the reactants, with no contamination from external sources. Furthermore, 4Ni/Zn-Co PBAs underwent four cycles of durability testing (Fig. 2g, Fig. S4 and Table S5 in Supporting information) and structural stability testing (Fig. S5 in Supporting information). The results demonstrated that the CO_2 reduction process on 4Ni/Zn-Co PBAs strictly followed a first-order reaction kinetics model, with product yields increasing proportionally over equal time intervals. Additionally, both the crystalline structure and light absorption capacity remained unchanged. These findings highlight the excellent performance stability and structural sustainability of the Ni/Zn-Co PBAs cubic S-scheme photocatalyst, providing a foundation for potential industrial applications.

Outstanding photocatalytic performance requires excellent charge separation. So, we examined the optical properties and band positions of five Co-based PBAs photocatalysts (Figs. S6 and S7 in Supporting information). The results showed that the band positions of Zn-Co PBAs and Ni-Co PBAs perfectly match the S-scheme charge transport mechanism requirements. Hence, we speculate that Ni/Zn-Co PBAs photocatalysts have an S-scheme charge transport path. To ascertain the S-scheme oriented migration pathway in Ni/Zn-Co PBAs photocatalysts, *in-situ* XPS characterization was performed on Zn-Co PBAs, Ni-Co PBAs, and Ni/Zn-Co PBAs (Figs. 3a-c and Fig. S8 in Supporting information). After constructing Ni/Zn-Co PBAs on a Zn-Co PBAs base, the Zn 2p binding energy shifted slightly in the direction negative, but this was offset by a larger positive change upon light-exposure, with Ni 2p showing the opposite trend. Before illumination, the binding energy changes were due to band bending from the Fermi-level equalization when Zn-Co PBAs and Ni-Co PBAs made contact [24–27]. This caused electrons and holes to gather on the surfaces of Zn-Co PBAs and Ni-Co PBAs respectively [28]. Upon light exposure, the bent bands formed a stable interfacial electric field at the Zn-Co PBAs and Ni-Co PBAs interface. This directed electrons to transfer from the oxidative photocatalyst to the reductive photocatalyst. The post-illumination binding energy changes of Zn 2p and Ni 2p fully confirmed the S-scheme charge transport mechanism hypothesis in Ni/Zn-Co PBAs photocatalysts. The S-scheme heterojunction formation and charge transport process are illustrated in Fig. S9 (Supporting information).

In the field of photocatalytic materials, the separation efficiency of photogenerated charges is one of the key factors determining the photocatalytic performance of materials. As a powerful characterization method, transient photovoltage spectroscopy can capture the dynamic behavior of photogenerated charge in materials in a time resolved manner, which provides an intuitive and accurate

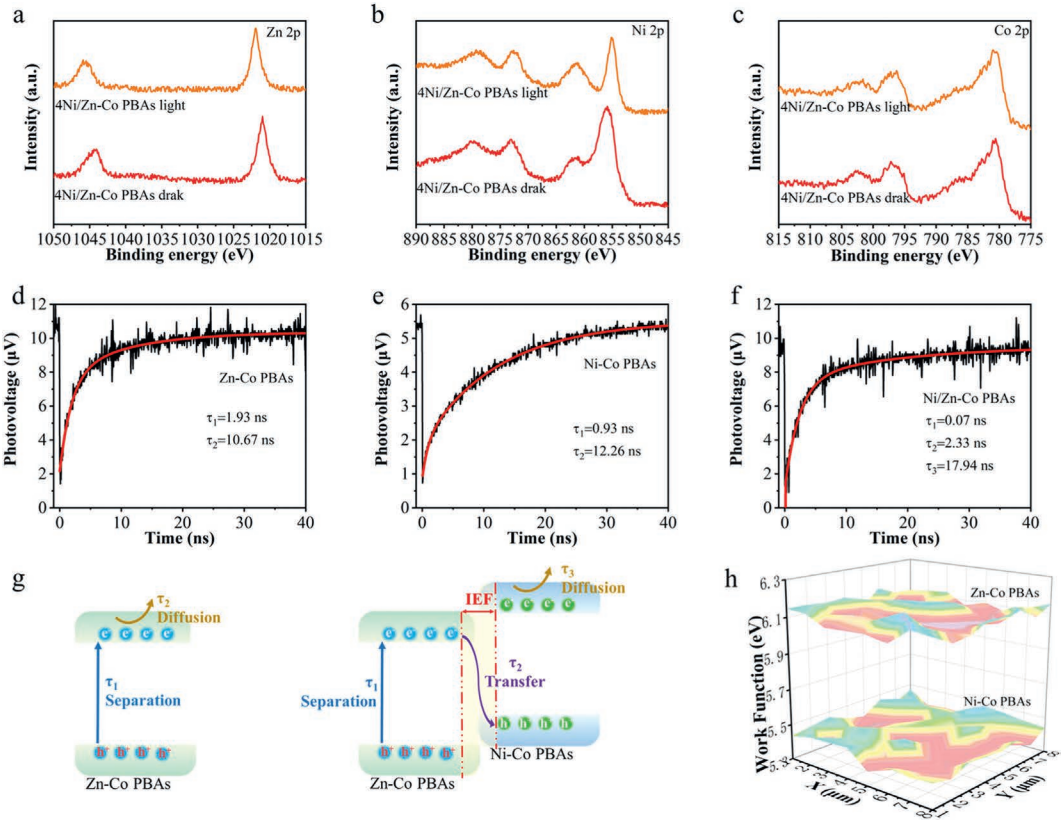


Fig. 3. The XPS spectra of (a) Zn, (b) Ni and (c) Co of 4Ni/Zn-Co PBAs. TPV spectra of (d) Zn-Co PBAs, (e) Ni-Co PBAs, and (f) 4Ni/Zn-Co PBAs. (g) The oriented migration pathway of photoexcited charges and (h) scanning Kelvin probe maps of PBAs photocatalysts.

experimental basis for further exploring the separation process of photogenerated charge. Exponential fitting of transient photovoltage spectrum is an important method to analyze the lifetime characteristics of photogenerated charge. In this analytical framework, different time constants (τ) correspond to the lifetime of photogenerated charges in different physical processes. τ_1 reflects the initial separation process of photogenerated charge at the moment of light excitation, which involves the generation of electron hole pairs excited by photon energy and their preliminary separation in a very short time. For a single photocatalyst, τ_2 describes the diffusion process of the separated photogenerated charge on the surface of the material, which directly affects whether the photogenerated charge can effectively participate in the surface catalytic reaction. For composite photocatalysts, τ_2 characterizes the directional migration behavior of photogenerated charges between the interfaces of different materials, which is very important for the efficient separation and utilization of charges. τ_3 is specific to composite photocatalysts, representing the effective life of photogenerated charges on the surface of materials, which determines the time window for photogenerated charges to participate in catalytic reactions on the surface. We also verified the electron transport path under the S-scheme mechanism by examining the electron lifetime (Figs. 3d-g). Single component samples fit a bi-exponential model, indicating two electron transfer routes. The first transfer phase (τ_1) resulted from intrinsic excitation of the single component photocatalyst upon light exposure, where induced electrons from the VB to CB, forming a Coulombic field. The second phase (τ_2) was due to some CB electrons migrating from the bulk to the surface, creating a local field. In contrast, the composite sample (Ni/Zn-Co PBAs) required tri-exponential fitting. Here, τ_2 represented the interfacial charge-transfer duration, and τ_3 represented the electrons diffusion duration. The significantly prolonged electron diffusion lifetime in Ni/Zn-Co PBAs suggests that the built-in electric field enabled effective electron-hole separation, thus markedly extending the photogenerated electrons effective duration. The work functions of Zn-Co PBAs and Ni-Co PBAs (Fig. 3h) also supported the directed electron transport.

To more intuitively see the electron transport results, EPR tests with DMPO as a molecular probe were carried out on Zn-Co PBAs, Ni-Co PBAs, and Ni/Zn-Co PBAs (Fig. S10 in Supporting information). As the CBs of Zn-Co PBAs and Ni-Co PBAs meet the O_2 activation condition, the enhanced $^{\bullet}O_2^-$ signal is attributed to effective charge separation allowing more electrons for O_2 activation [29]. Importantly, the $^{\bullet}OH$ signal changed significantly. Since the VB of Ni-Co PBAs cannot effectively activate OH groups, the increased $^{\bullet}OH$ signal in Ni/Zn-Co PBAs entirely depends on Zn-Co PBAs [30]. If the charge transport mode in Ni/Zn-Co PBAs didnot follow the S-scheme mechanism, charges would gather on the VB of Ni-Co PBAs, contradicting the experimental results. Thus, Ni/Zn-Co PBAs photocatalysts are confirmed to follow the S-scheme charge transport mechanism, a detailed schematic is in Fig. S11 (Supporting information). Single-wavelength laser excitation of Zn-Co PBAs, Ni-Co PBAs, and Ni/Zn-Co PBAs again showed that only simultaneous excitation of Zn-Co PBAs and Ni-Co PBAs enhances photoinduced charge separation efficiency, consistent with all previous S-scheme mechanism characterization results (Fig. S12 in Supporting information) [31]. Fig. S13 (Supporting information) verifies from photophysical, photochemical, and photoelectrochemical perspectives that the S-scheme system improve the charge separation efficiency of Ni/Zn-Co PBAs photocatalysts.

According to the S-scheme mechanism, the electrons of the Ni/Zn-Co PBAs photocatalyst should eventually be enriched on the CB of the Ni-Co PBAs. Therefore, the Ni/Zn-Co PBAs photocatalyst is expected to exhibit a stronger CO_2 activation ability. As

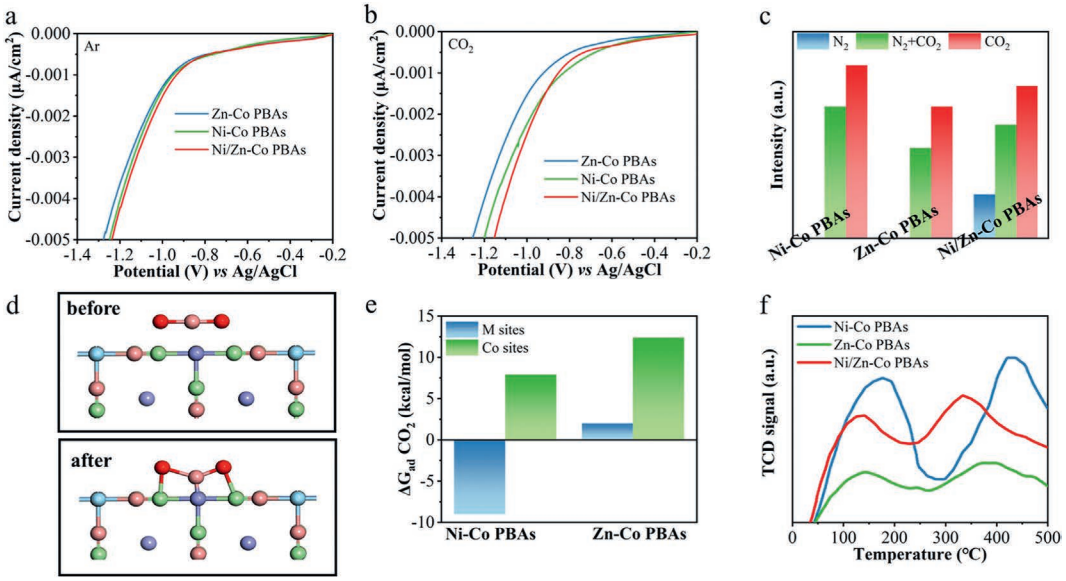


Fig. 4. (a, b) Electrochemical reduction curves and (c) SS-SPS response intensities under different atmospheres of PBAs photocatalysts. (d) Optimized CO_2 adsorption structures and (e) CO_2 adsorption free energy diagram of different sites. (f) CO_2-TPD profiles of PBAs photocatalysts.

depicted in Figs. 4a and b, compared with Ar atmosphere, both single-component photocatalysts and the composite photocatalyst demonstrate enhanced redox capabilities under CO_2 atmosphere, with the Ni/Zn-Co PBAs showing the most remarkable performance [32]. This observation effectively underscores the advantageous effect of the S-scheme mechanism in elevating the redox capabilities of the photocatalytic system. Analogous outcomes are also discernible in the atmosphere-regulated SS-SPS measurements (Fig. 4c and Fig. S14 in Supporting information). Specifically, under a N_2 atmosphere, the single-component photocatalysts exhibit no photocurrent signals. This stems from the absence of charge separation in the absence of electron and hole scavengers. In stark contrast, the Ni/Zn-Co PBAs photocatalyst is not constrained by this limitation. This is because the photoinduced charges can migrate across the interface between Zn-Co PBAs and Ni-Co PBAs, thereby generating measurable photocurrent signals. Most revealingly, upon the incremental introduction of CO_2 into the detection setup, the photocurrent signals for all materials undergo a notable enhancement, and this enhancement is positively correlated with the concentration of CO_2. This serves as compelling evidence that CO_2 functions as an electron scavenger, effectively facilitating electron transfer, and by extension, underscoring the electrons' pronounced capacity to activate CO_2 [33,34].

In order to conduct a more rational investigation into the CO_2 activation capabilities of different materials, particularly attention was devoted to the metal sites involved in the activation process. To this end, DFT calculations were employed to determine the Gibbs free energy associated with the CO_2 molecules adsorbed onto various metal sites (Figs. 4d and e). The simulation results reveal that when CO_2 molecules are adsorbed onto metal sites, the adjacent N atoms form new N-O bonds with the O atoms in CO_2. Consequently, the linear configuration of the CO_2 molecule is distorted into a triangular geometry. The CO_2 adsorption free energy values onto Zn^{2+} or Co^{3+} sites are positive, signifying that CO_2 can readily desorb from these sites. In marked contrast, the CO_2 adsorption free energy onto Ni^{2+} sites are negative. Hence, CO_2 capture at Ni^{2+} centers proceed with notable spontaneity, allowing gas molecules to readily anchor onto the Ni-Co PBA surface directly from the reaction medium [35,36]. Furthermore, CO_2-TPD (CO_2-temperature programmed desorption) experiments (Fig. 4f) were conducted to evaluate the CO_2 adsorption capacity. The results demonstrate that Ni^{2+} sites exhibit the most significant enhancement in CO_2 adsorption capability, irrespective of whether it is physical adsorption in the low-temperature region or chemical adsorption in the medium- and high-temperature regions [37]. This conclusion is further corroborated by *in-situ* diffuse reflectance infrared Fourier transform spectroscopy (DRIFTS) spectra (Fig. S15 in Supporting information).

The reaction mechanism of CO_2 photoreduction was explored using both *in-situ* DRIFTS spectra (Figs. 5a and b), NAP-XPS (near-ambient pressure X-ray photoelectron spectroscopy) spectra (Fig. 5c) and DFT calculations (Fig. 5d). In the *in-situ* DRIFTS spectra, by comparing with other materials and literature, the generation of carbonates and bicarbonate: Fig. 5a shows the infrared characteristic peaks dominated by CO_2 and CO_3^{2-} stretching vibration mode in the ranges of 1420, 1647, 1538 and 1556 cm^{-1} [38,39]. The infrared characteristic peaks within this range are mainly attributed to four different stretching vibration modes: adsorbed bidentate carbonate, multidentate carbonate or hydrogen carbonate adsorbed on Ni^{2+} sites, multidentate carbonate adsorbed on Ni^{2+} sites, and δ(COH) band of hydrogen carbonate. The generation of formic acid: There are many infrared characteristic peaks of formic acid, but most of the stretching vibration mode infrared peaks of C=O bands coincide with the infrared characteristic peaks of carbonates or hydrogen carbonates. Therefore, the independent 2δ(OCH) band stretching vibration mode in the range of 1587, 1620 and 1702 cm^{-1} was selected as the basis for judging the generation of formic acid [40,41]. The center position of the characteristic peak of 2δ(OCH) band stretching vibration gradually shifts towards higher wave numbers, indicating the emergence of new bands with vibration peaks at larger wave numbers during formic acid generation. It is generally believed that there are three types of 2δ(OCH) bands. The vibration peaks of type I and II appear at lower wave numbers, corresponding to some formic acid bound to non-metallic vacancies, while the type III formic acid with the highest wave number is bound to Ni^{2+}. Due to the formation of formic acid being the main rate limiting step of CO_2 reduction reaction, formic acid should mainly form in an atmosphere with a more active chemical environment. Therefore, it has been demonstrated that the Ni/Zn-Co PBAs system with Ni^{2+} as the adsorption and activation center has significant reaction advantages. The generation of CO: The infrared characteristic peaks observed in Fig. 5b

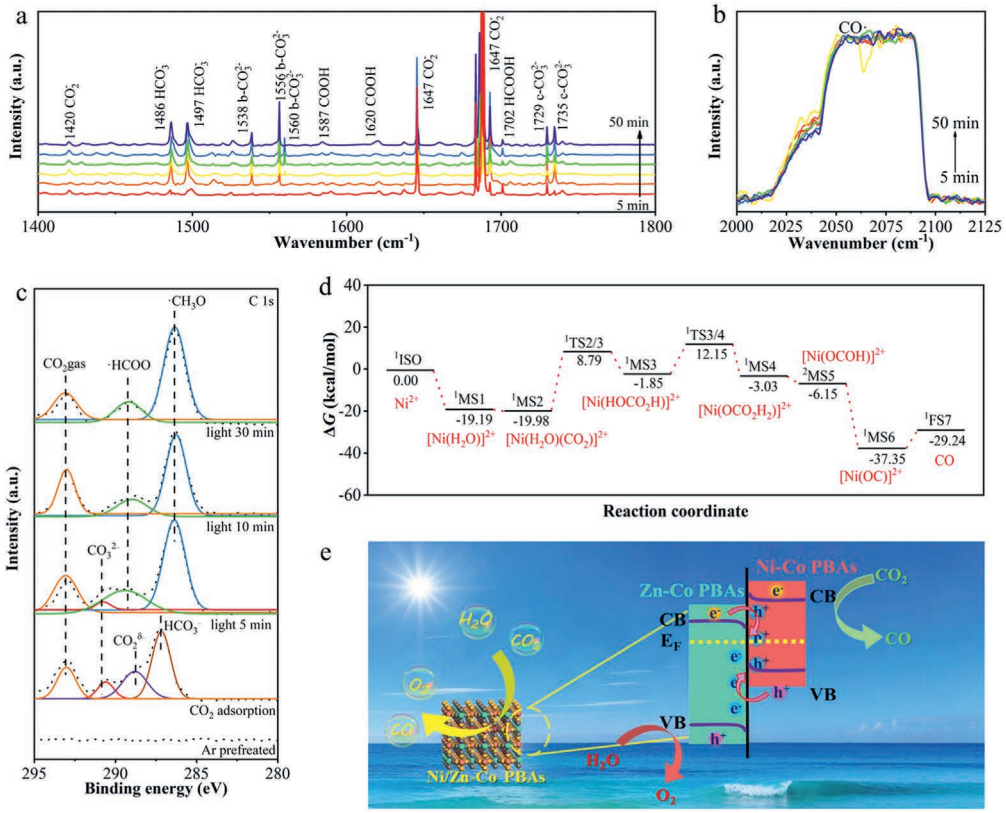


Fig. 5. (a, b) *In-situ* DRIFTS spectra of CO_2 reduction. (c) NAP-XPS spectra over Ni/Zn-Co PBAs. (d) Calculated Gibbs free energy diagrams for photocatalytic CO_2 reduction reaction. (e) Schematic diagram of oriented charge transfer and reaction in the Ni/Zn-Co PBAs S-scheme system.

(2000–2125 cm^{-1}) correspond to the vibrational stretching mode of CO adsorbed at the top of the metal site [42].

Fig. 5c depicts the NAP-XPS C 1s spectra of CO_2 conversion over Ni/Zn-Co PBAs at different illumination times. After Ar pretreatment during CO_2 adsorption, the C 1s spectrum primarily exhibits peaks from adsorbed CO_2 species like CO_2 gas, CO_2^-, CO_3^{2-}, and HCO_3^-. As illumination progresses, the binding energy peaks of these species weaken, while features assignable to $HCOO^•$ and $CH_3O^•$ intermediates emerge and strengthen [43]. This suggests that CO_2 is photoreduced to $HCOO^•$ intermediates on the catalyst surface, echoing DRIFTS results. The formation and transformation of these intermediates offer key insights into the CO_2 reduction mechanism.

The Gibbs free energy profiles of key photocatalytic CO_2 reduction intermediates, calculated *via* DFT, are displayed in Fig. 5d. The reaction pathway commences with CO_2 adsorption, traversing multiple intermediates and transition states route to CO generation. Notable energy fluctuations across the pathway reveal several energy barriers. For example, the energy change transitions from $Ni(H_2O)^{2+}$ to $Ni(H_2O)(CO_2)^{2+}$ at −19.19 kcal/mol, then *via* transition state ^{1}TS2/3 and intermediate ^{1}MS3, followed by intermediate ^{1}TS3/4 and ^{1}MS4, culminating in CO formation at -29.24 kcal/mol. These energy barriers pinpoint potential rate-determining steps in the reaction. Fig. 5e schematically illustrates the mechanism of CO_2 photocatalytic reduction to CO on designed Ni/Zn-Co PBAs. Under illumination, charges are generated and separated in the semiconductor. Electrons transfer from the VB to the CB, then migrate between Ni-Co PBAs and Zn-Co PBAs *via* an S-scheme mechanism. The transferred electrons, under the action of Ni^{2+} sites, drive CO_2 reduction to CO. Meanwhile, holes trigger water oxidation to O_2.

In this study, we successfully developed a Ni/Zn-Co PBAs S-scheme heterojunction photocatalyst for efficient CO_2 reduction. The Ni/Zn-Co PBAs prepared by *in-situ* growth method with Zn-Co PBAs as the core and Ni-Co PBAs as the shell, effectively promoted charge transfer and separation. This photocatalyst achieved a CO_2 conversion yield of ~38 μmol g^{-1} h^{-1}, outperforming many recently reported systems. Our experimental results confirmed that the Ni/Zn-Co PBAs followed an S-scheme charge transfer mechanism and demonstrated strong CO_2 adsorption and activation abilities. *In-situ* methods further revealed the dynamic process of CO_2 reduction, including the formation of intermediates such as $HCOO^-$ and HCO_3^{2-} and their final conversion to CO. Overall, this work offers new insights into designing high-performance PBAs-based S-scheme heterojunctions to enhance CO_2 reduction efficiency, providing an important reference for advancing sustainable carbon utilization technologies and achieving carbon neutrality.

CRediT authorship contribution statement

Enqi Zhang: Writing – original draft, Visualization, Validation, Investigation, Formal analysis, Data curation, Conceptualization. **Fanyu Kong:** Writing – original draft, Visualization, Validation, Investigation, Formal analysis, Data curation, Conceptualization. **Lina Dai:** Visualization, Validation, Data curation. **Xianglan Dong:** Visualization, Validation, Data curation. **Hongquan Jiang:** Writing – review & editing, Supervision, Formal analysis, Conceptualization. **Yanduo Liu:** Writing – review & editing, Supervision, Funding acquisition, Formal analysis, Conceptualization. **Yang Qu:** Writing – review & editing, Supervision, Formal analysis, Conceptualization.

Declaration of competing interest

The authors declare that they have no known competing financial interests or personal relationships that could have appeared to influence the work reported in this paper.

Acknowledgment

The authors acknowledge support from the National Natural Science Foundation of China (No. U24A2071) to Y.D. Liu.

Supplementary materials

Supplementary material associated with this article can be found, in the online version, at doi:10.1016/j.cclet.2026.112479.

References

[1] J, D. Li, Y.M. Ma, et al., Chin. Chem. Lett. 36 (2025) 111394.
[2] H.Y. Xiang, J. Lopez, T. Hu, et al., Comp. Funct. Mat. 1 (2025) 20250102.
[3] H. Li, C.L. Gao, G. Yang, et al., Chin. Chem. Lett. 36 (2025) 110547.
[4] J.D. Li, Y. Qu, Y.D. Liu, et al., Sep. Purif. Technol. 354 (2024) 126761.
[5] Y.D. Liu, Y.H. Chen, W.B. Jiang, et al., Research 2022 (2022) 9831340.
[6] X.F. Wang, H.Q. Jiang, Y.D. Liu, et al., Mater. Lett. 147 (2015) 72–74.
[7] W.W. Liu, J. Pan, R.F. Peng, et al., Rare Met. 40 (2021) 3554.
[8] P. Xu, T.Z. Hao, Z.T. Liu, et al., Chin. Chem. Lett. 36 (2025) 110899.
[9] D, H. Huang, T.F. Wu, D.Y. Xie, et al., Comp. Funct. Mat. 1 (2025) 20250104.
[10] Y. Huang, J.F. Zhang, O. Ruzimuradov, et al., Comp. Funct. Mat. 1 (2025) 20250103.
[11] C. Yang, Q.H. Zhang, W. Wang, et al., Sci. China Mater. 67 (2024) 1830–1838.
[12] Y. He, P.Y. Hu, J.Y. Zhang, et al., ACS Catal. 14 (2024) 1951–1961.
[13] B.C. Zhu, C.J. Jiang, J.S. Xu, et al., Mater. Today 82 (2025) 251–273.
[14] M.J. Xu, Q. Zhang, Z.Q. Zhu, et al., J. Cleaner Prod. 377 (2022) 134258.
[15] G. Li, R.Y. Tan, B.H. Gao, et al., Carbon 228 (2024) 119315.
[16] Y.X. Shi, B. Yang, G.J. Song, et al., J. Colloid Interface Sci. 673 (2024) 807–816.
[17] S. Cheng, C. Shen, H. Zheng, et al., Appl. Catal. B: Environ. 269 (2020) 118785.
[18] R.N. Guo, Y. Chen, Y. Yang, et al., Chin. Chem. Lett. 34 (2023) 107837.
[19] Y. Huang, J. Ge, H. Chen, et al., Ensor. Actuat. B: Chem. 327 (2021) 128871.
[20] L. Shen, Q. Zhang, J. Luo, et al., Appl. Surf. Sci. 551 (2021) 149360.
[21] Y.C. Pi, H. Lin, Z.Y. Meng, et al., Chem. Eng. J. 499 (2024) 155618.
[22] K.K. Yao, J.N. Li, S. Yuan, et al., J. Mater. Chem. C 10 (2022) 244–250.
[23] X.Y. Wu, Y. Ru, Y. Bai, et al., Coord. Chem. Rev. 451 (2022) 214260.
[24] F. Li, X.Y. Yue, Y.L. Liao, et al., Nat. Commun. 14 (2023) 901.
[25] S.Y. Yue, R. Li, Z.R. Wei, et al., Chin. J. Catal. 71 (2025) 353–362.
[26] Y.F. Zhang, S. Wang, Chin. J. Catal. 71 (2025) 1–4.
[27] L. Fang, L.E. Bai, D. Wu, et al., Chem. Eng. J. 510 (2025) 161820.
[28] Y. Chen, F. Yang, J.R. Duan, et al., Chem. Eng. J. 514 (2025) 163380.
[29] Z.C. He, Y. Liu, Z. Li, et al., Appl. Catal. B: Environ. 355 (2024) 124207.
[30] X. Guo, X.J. Sun, Z.Y. Wang, et al., Fuel 343 (2023) 128004.
[31] L.N. Dai, X.L. Dong, E. Zhang, et al., Fuel 396 (2025) 135297.
[32] L.N. Dai, H. Wang, Y.D. Liu, et al., Chem. Eng. J. 512 (2025) 162380.
[33] X.J. Zhang, Y.D. Liu, L.Q. Chen, et al., Appl. Catal. B: Environ. 282 (2021) 119563.
[34] Y.D. Liu, X.J. Zhang, J. Bian, et al., Appl. Catal. B: Environ. 254 (2019) 260–269.
[35] L.N. Dai, H. Wang, L.R. Cui, et al., Renew. Energy 247 (2025) 123093.
[36] L.N. Dai, Q. Li, X.L. Dong, et al., Fuel 395 (2025) 135210.
[37] Y.D. Liu, X.Y. Li, K. Ferdi, et al., ACS Mater. Lett. 7 (2025) 1144–1151.
[38] X.J. Zhang, Y.D. Liu, L.Q. Chen, et al., Small Struct. 3 (2022) 2200011.
[39] Y.D. Liu, M.W. Li, J.N. Guo, et al., J. Colloid Interface Sci. 667 (2024) 23–31.
[40] X. Guo, Z.Y. Wang, S.Q. Jiang, et al., Fuel 367 (2024) 131504.
[41] Y.D. Liu, J.D. Li, X.L. Dong, et al., Inorg. Chem. Front. 11 (2024) 5310–5318.
[42] Y. Yin, X.L. Dong, L.N. Dai, et al., Sep. Purif. Technol. 358 (2025) 130393.
[43] Q.H. Liu, X. Guo, Y.F. Hu, et al., Sep. Purif. Technol. 360 (2025) 130920.